Power expectation as a unified metric for the evaluation of vibration energy harvesters

Camille Saint-Martin, Adrien Morel, Ludovic Charleux, Émile Roux, Aya Benhemou, Adrien Badel

HAL Id: hal-03737305

https://hal.science/hal-03737305

Submitted on 24 Jul 2022

Power expectation as a unified metric for the evaluation of vibration energy harvesters

Saint-Martin, C.[a,*], Morel, A.[a], Charleux, L.[a], Roux, E.[a], Benhemou, A.[a], Badel, A.[a]

[a]Univ Savoie Mont Blanc, SYMME, F-74000, Annecy, France

Abstract

Vibration energy harvesters (VEHs) allow the extraction of ambient mechanical energy. The proposed analysis focuses on bistable harvesters with Duffing nonlinearity. Bistable harvesters exhibit larger frequency bandwidth than linear monostable harvesters, but they exhibit complex behaviors (i.e., multiple periodic orbits and chaos), making their evaluation challenging. To assess the quality of a VEH, it is necessary to evaluate its energy performance generically. In this paper, we offer a new quantitative metric that can be used to evaluate bistable harvesters while taking into account the richness and diversity of their dynamics. This metric – called *power expectation* – is based on the average harvested power of each existing orbit weighted by its occurrence probability. The value of this power expectation depends on the harvester characteristics and potential orbit jump strategy implemented. Finally, we define a new figure of merit (FoM) based on the integral of the power expectation over all vibration frequencies. This FoM can be used for a generic evaluation of nonlinear vibration energy harvesters (NVEHs), by taking into account the various orbits and their respective probability of occurrence depending on the orbit jump strategy used. The proposed FoM also makes it possible to ensure a fair comparison with linear VEHs and quantitatively assess the effectiveness of orbit jump strategies for a given VEH.

Keywords: vibration energy harvesting, bistable oscillator, piezoelectric energy harvester, nonlinear dynamics, figure of merit

1. Introduction

Vibration energy can be scavenged with piezoelectric energy harvesters (PEHs) to replace or complement batteries in low-power electronic systems [1]. A PEH is traditionally composed of a linear mechanical oscillator that amplifies the vibrations when excited around its natural frequency. Fig. 1(a) shows the power-frequency response of a linear-type harvester excited by a sinusoidal vibration. As shown in Fig. 1(a), such a linear PEH exhibits a narrow frequency bandwidth. Therefore, a slight mismatch between the vibration frequency and the linear PEH resonant frequency drastically decreases the harvested power. This constitutes a major problem in environments where the vibrations are time-varying or random [2, 3]. During the last decade, NVEHs have been attracting research interest because of their enhanced frequency bandwidth compared to their linear counterparts [4, 5]. However, NVEHs exhibit complex dynamical behaviors making their evaluation and comparison challenging [6, 7, 8]. Here, we offer a new metric that assesses the performances of NVEHs while taking into account the full complexity of their nonlinear behaviors.

There has been a long-standing interest on NVEHs for their broadband behavior [9] (for review, see e.g. [10]). The nonlinear behavior of such harvesters may come from their structure or from the nature of the involved forces (e.g. electromagnetic or elastic) [11]. Among nonlinear harvesters, Duffing-type harvesters with bistable nonlinearity have been attracting research interest for many years because they exhibit broadband power-frequency responses (for review, see e.g. [12]). There has been tremendous research ef-

forts in order to understand [13], exploit [14], and improve [15, 16, 17] the behavior of multistable NVEH. Compared to linear PEH, the complexity of NVEH behaviors makes their evaluation more challenging. Indeed, such harvesters can exhibit multiple stable operating limit cycles – called *orbits* – depending on their initial conditions (ICs) [18, 19]. Some of these orbits – namely the high orbits for which the inertial mass moves from one well to the other – exhibit advantageous power-frequency behaviors and are interesting for energy harvesting [9, 6, 7]. However, some other orbits, namely the low orbits for which the inertial mass oscillates around a single well, exhibit low harvested power performances. In order to force high orbit operation of NVEH and take advantage of the full NVEH potential, it is necessary to implement orbit jump strategies [20, 21]. For instance, such orbit jumps can be performed with impact-induced method [22], wind-induced method [23], buckling level modification [24, 25], voltage impulse perturbation [5], load perturbation [26], or by using stochastic resonance phenomena [27]. While many NVEHs and orbit jump strategies have already been implemented in the literature, there is still a need for a quantitative metric and an FoM to compare and assess the quality of nonlinear harvesters associated with a given orbit jump strategy. As illustrated in Table 1, various FoMs have already been proposed in the literature. For instance, some FoMs are used to compare linear PEHs and consist in the product of the maximum power times the frequency bandwidth of the harvester [28, 29] or the integral of the power over all the vibration frequencies [30, 31]. Such FoMs can easily be estimated for linear PEH because they present a single periodic regime – of probability of occurrence equal to 1 – as shown in Fig. 1(a). Because of the variety of dynamical phenomena that can be found in NVEH (e.g., co-existing orbits, subharmonic behaviors [32], and chaos [33, 34]), the linear PEH FoM cannot be directly transposed to compare NVEH. As shown in Table 1, an FoM has been proposed to evaluate and compare the performances of NVEH in [35] but rely on sweep excitations. Figure 1(b) shows the power curve of an NVEH excited by

sweep excitation [35]. With this method, one can observe two different orbits. The probabilities of occurrence of these orbits are assumed to be equal in [35] (meaning that there is 50% chance of being on the highest orbit, and 50% chance of being on the lowest orbit). However, in practice, there are many more orbits than the two orbits considered, and the respective probabilities of these orbits are not equal to 50%, and depend on the level of excitation and on the vibration frequency. Figure 1(c) illustrates the multiple orbits toward which an NVEH can stabilize and their associated probability of occurrence (for a given excitation amplitude). Figure 1(c) proves that an FoM based on sweep excitation is insufficient to establish a global assessment of an NVEH, does not correspond to most real applicative cases, and hinders some of the aforementioned dynamical phenomena. Furthermore, such FoMs do not enable any comparison of orbit jump strategies which are still vital for NVEH.

As shown in Table 1, this paper introduces the power expectation, noted $\overline{P}$, and defines an FoM, noted $\text{FoM}_{\overline{P}}$, based on it. This power expectation is obtained from the average harvested power of each orbit pondered by its probability of occurrence obtained with a given orbit jump strategy. As described in Table 1, $\text{FoM}_{\overline{P}}$ makes it possible to perform a quantitative evaluation of an NVEH and its associated orbit jump strategy, while taking into account its complex dynamic behaviors, and enables the fair comparison of linear and nonlinear energy harvesting solutions. Furthermore, $\text{FoM}_{\overline{P}}$ can be applied to any harvesters regardless of their transduction mechanism (e.g., piezoelectric or electromagnetic).

Section 2 recalls the model of a Duffing-type VEH as well as its dynamical behaviors, trajectories, and orbits. Thereafter, we justify in section 3 the choice of an ICs grid that ensures the detection of all orbits for all vibration frequencies. In section 3, the harvested power and the probability of occurrence associated with a given orbit are provided. Then, based on a grid of given ICs, we introduce the mathematical expression of the power expectation based on the probability of occurrence of each orbit and show its relevance for the evaluation

2

FoM	Authors	Reference	Volume	Probability	Subharmonic	Bandwidth	P_{max}	Part of the system that is evaluated
SFoM_{BW}	Liu et al.	[35]	✓	✗	✗	✓	✓	Nonlinear PEH
FoM_{strat}	Morel et al.	[31]	✗	✗	✗	✓	✓	Interface circuits
NPD	Beeby et al.	[36]	✓	✗	✗	✗	✓	Linear PEH
FOM	Cai et al.	[29]	✗	✗	✗	✓	✓	Interface circuits
FoM_v	Mitcheson et al.	[37]	✓	✗	✗	✗	✓	Linear PEH
FoM_{BW}	Mitcheson et al.	[37]	✓	✗	✗	✓	✓	Linear PEH
$\text{FoM}_{\overline{P}}$	This paper		✗	✓	✓	✓	✓	Nonlinear PEH + orbit jump strategy

Table 1: Table of comparison with other FoMs from literature. SFoM_{BW} (Systematic Figure of Merit with Bandwidth information), FoM_{strat} (strategy Figure of Merit), NPD (Normalized Power Density), FOM = Bandwidth of the output power over natural bandwidth of the transducer, FoM_v (volume Figure of Merit), FoM_{BW} (bandwidth Figure of Merit).

of the performance of an NVEH. We discuss several examples of orbit jump strategies to illustrate their impact on the power expectation values. Comparing the expectation of harvested power for each orbit jump strategy makes it possible to gauge their quality. In section 4, we define $\text{FoM}_{\overline{P}}$ – based on the power expectation – that enables the unified evaluation of NVEH by taking into account the implemented orbit jump strategy. Based on $\text{FoM}_{\overline{P}}$, three fictive orbit jump strategies associated with the same nonlinear energy harvester are quantitatively compared. Then, the influence of the level of acceleration on the power expectation and FoM is studied, with each of the aforementioned orbit jump strategies. Finally, in section 5, the $\text{FoM}_{\overline{P}}$ is computed in order to evaluate the effectiveness of an orbit jump strategy inspired from the literature.

2. Electromechanical dynamics of NVEH

In this section, a description of the electromechanical dynamics of NVEH is given. Then, a detailed description of the dynamics and orbit classification are provided.

2.1. Model of bistable NVEH

First, we consider a model of a Duffing oscillator including piezoelectric material, forced by a sinusoidal excitation, and connected to an extraction circuit. The model of such an NVEH is given in (1).

$$\begin{cases} \ddot{x} = -\frac{\omega_0^2}{2}\left(\frac{x^2}{x_0^2} - 1\right)x - \frac{\omega_0}{Q}\dot{x} - \frac{1}{M}f(x,v) + A\sin(2\pi f_d t) & \text{(1a)} \\ \\ \dot{v} = \frac{1}{C_p}f(x,\dot{x}) - \frac{1}{RC_p}v & \text{(1b)} \end{cases}$$

Where x represents the position of the mass M, $\dot{x}$ is the speed of the mass and $\ddot{x}$ corresponds to mass acceleration. The oscillator has two stable positions for $x = \pm x_0$. The linearized behavior for small oscillations around $x \approx x_0$ exhibits a natural angular frequency ω_0 and a mechanical quality factor Q as defined in [38]. The oscillator is submitted to a sinusoidal excitation of constant amplitude $A = 2.5$ m.s^{-2} and frequency f_d. The function $f : \mathbb{R}^2 \xrightarrow{C^1} \mathbb{R}$ depends on the PEH architecture used. (1a) expresses the mechanical dynamics with a term depending on voltage v and displacement x. (1b) models the electrical dynamics with a term depending on mechanical displacement x and its first derivative. In this study, the focus is on the particular case of the buckled-beam NVEH reported in [24]. Nevertheless, the approach presented in this paper is generalizable and can be applied to any VEH. The harvester considered is shown in Fig. 2. For this harvester, the expression of f is given in [24]. The dynamics of this harvester is modeled by (2).

$$\begin{cases} \ddot{x} = -\frac{\omega_0^2}{2}\left(\frac{x^2}{x_0^2} - 1\right)x - \frac{\omega_0}{Q}\dot{x} - 2\frac{\alpha}{ML}xv + A\sin(2\pi f_d t) & \text{(2a)} \\ \\ \dot{v} = 2\frac{\alpha}{LC_p}x\dot{x} - \frac{1}{RC_p}v & \text{(2b)} \end{cases}$$
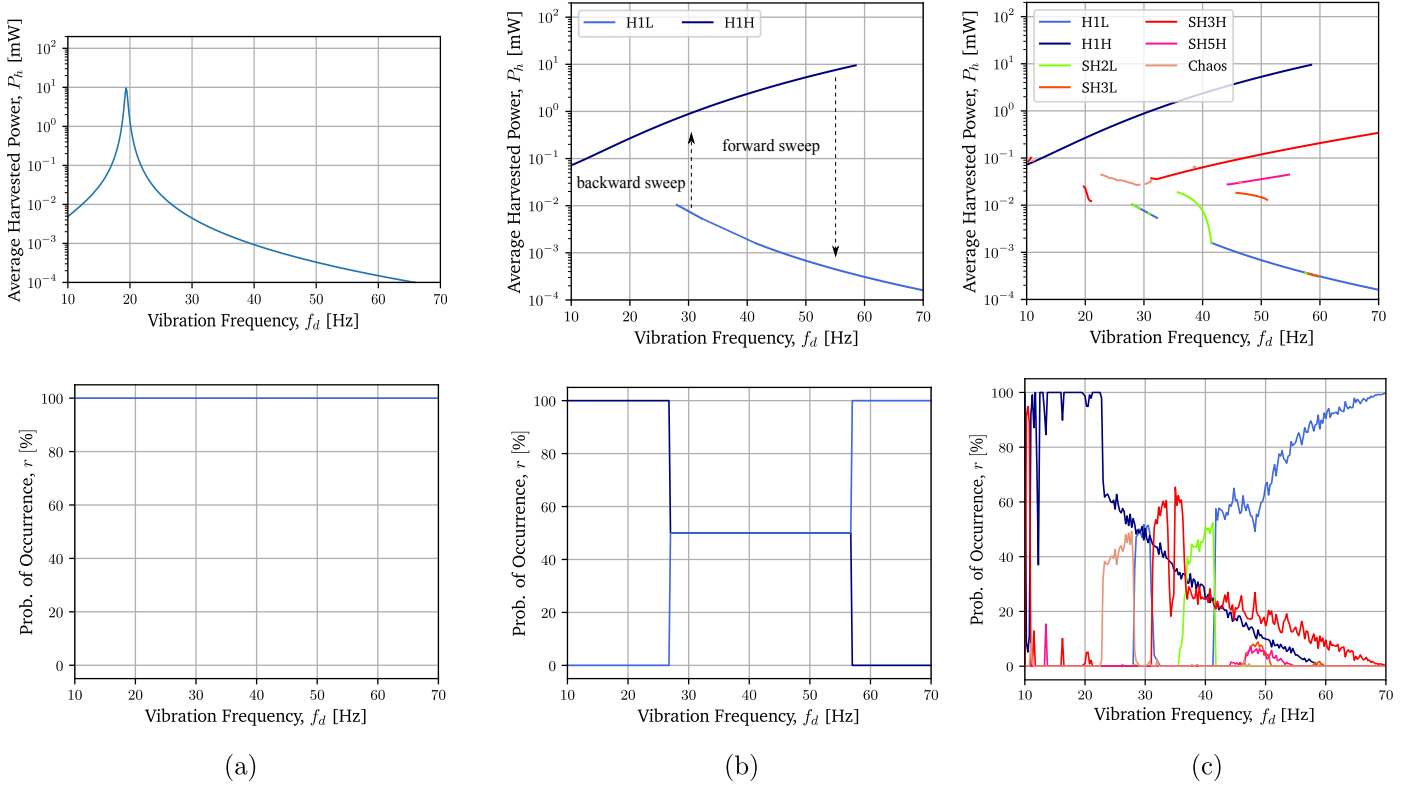
Fig. 1: Power versus frequency and probability of occurrence for (a) linear VEH, (b) NVEH with forward and backward sweeps, and (c) NVEH with subharmonic behaviors. The acronyms in (b,c) are defined in subsection 2.3.
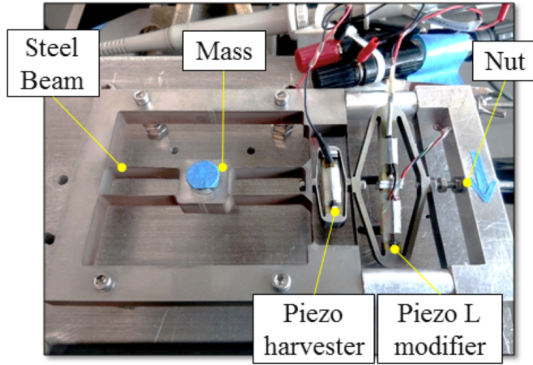

Fig. 2: Experimental NVEH from [32] with dynamics described by (2).
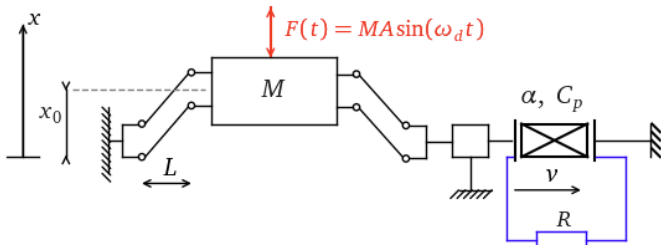

Fig. 3: Schematic representation of the bistable NVEH.

A schematic representation of the NVEH is given in Fig. 3. The oscillator consists in buckled steel beams with a length of L on which a mass M is fixed. α and C_p are the force factor and the clamped capacitance of the piezoelectric material, respectively. The harvested power corresponds to the one dissipated in the resistor R which represents the input impedance of the interface circuit. Parameter values of the NVEH considered are summarized in Table 2. Note that the value of $R = 1/C_p\omega_0$ is the one maximizing the harvested power at the resonant frequency of the NVEH linearized model, as explained extensively in section 4.1.

2.2. Orbits and chaos in NVEH dynamics

Equation system (2) is solved numerically from an initial state when $t = 0$, $\boldsymbol{X}(0) = \begin{pmatrix} x(0) & \dot{x}(0) & v(0) \end{pmatrix}^\top$. Figures 4(a) – 5(a) show time waveforms associated with four different initial states $\boldsymbol{X}^1(0)$, $\boldsymbol{X}^2(0)$, $\boldsymbol{X}^3(0)$ and $\boldsymbol{X}^4(0)$ for a vibration frequency $f_d = 25$ Hz. These multiple behaviors illustrate the diversity and complexity of the nonlinear dynamics

4

Parameters	Values	Units
x_0	0.5	mm
M	17.3	g
ω_0	121	rad.s^{-1}
Q	87	
α	0.068	N.V^{-1}
C_p	1.05	μF
R	7.83	kΩ

Table 2: Parameter values for the buckled-beam NVEH [24].
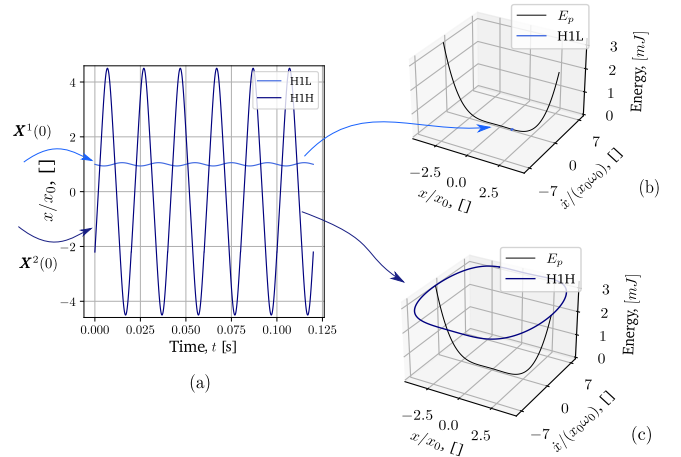

Fig. 4: (a) Harvester response time starting from $\boldsymbol{X}^1(0) = (4.98.10^{-4}, -9.37.10^{-3}, -2.76.10^{-2})^\top$ and $\boldsymbol{X}^2(0) = (-1.10.10^{-3}, 5.69.10^{-1}, -3.79)^\top$ and state-space representation of (b) H1L (c) H1H with $f_d = 25$ Hz. The acronyms H1H and H1L are defined in subsection 2.3.
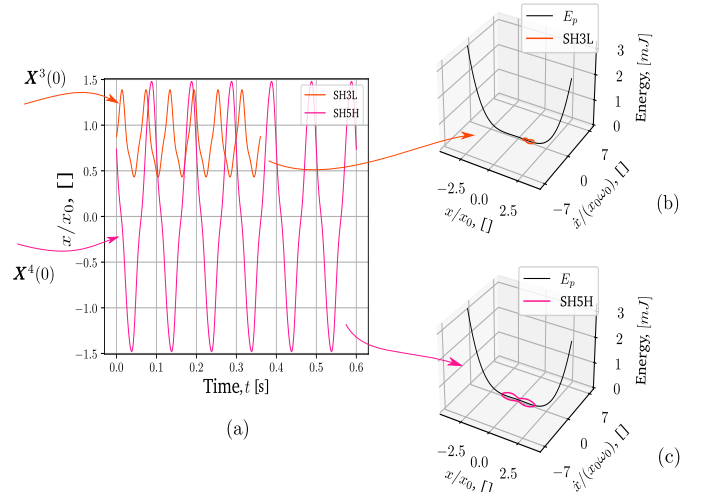
of (2). Orbit convergence depends on the IC of the numerical simulation. Figures 4(b, c) (resp. Figures 5(b, c)) show the potential wells of the bistable system and trajectories for two initial states in the $(x/x_0, \dot{x}/x_0\omega_0)$ phase plane, respectively. The analytical expressions of the elastic potential energy E_p, the kinetic energy E_k and the mechanical energy E_m are given by (3), (4) and (5).

$$E_p(x) = \frac{M\omega_0^2}{8x_0^2}(x + x_0)^2(x - x_0)^2 \quad (3)$$

$$E_k(\dot{x}) = \frac{1}{2}\dot{x}^2 \quad (4)$$

$$E_m(x, \dot{x}) = E_p(x) + E_k(\dot{x}) \quad (5)$$

The potential energy (3) presents two global minimum values at $x = \pm x_0$ and a local maximum at $x = 0$.

2.3. Orbit detection and classification with an ICs grid

For different initial states, we obtain different orbits that coexist for a given vibration frequency. This demonstrates the relevance of testing different ICs to observe the full richness of NVEH dynamics. A uniformly distributed grid of ICs $\boldsymbol{G}$ is defined on a compact subset $\boldsymbol{B} \subseteq \mathbb{R}^3$. The volume of the 3D grid is chosen in order to contain all existing orbits for each vibration frequency. We note $I \subset \mathbb{N}_0$ the index set.

$$\boldsymbol{G} = \left\{ (\boldsymbol{x}, \dot{\boldsymbol{x}}, \boldsymbol{v})^\top \mid (x^i, \dot{x}^i, v^i)^\top \hookrightarrow \mathcal{U}(\boldsymbol{B}), \ i \in I \right\} \quad (6)$$

Fig. 5: (a) Harvester response time starting from $\boldsymbol{X}^3(0) = (4.37.10^{-4}, 1.33.10^2, 1.69.10^{-1})^\top$ and $\boldsymbol{X}^4(0) = (3.68.10^{-4}, -4.70.10^{-2}, -5.27.10^{-1})^\top$ and state-space representation of (b) SH3L (c) SH5H with $f_d = 25$ Hz. The acronyms SH3L and SH5H are defined in subsection 2.3.

We assume that this grid enables the detection and observation of all existing orbits at each vibration frequency because its volume is sufficiently large and its discretization steps are sufficiently small in each direction. The choice of grid size and discretization steps must be defined beforehand performing preliminary dynamics studies. This is an important step for the qualitative analysis of the different existing orbits for each vibration frequency. For each vibration

5

frequency f_d, an ICs grid $\mathbf{G}$ of 8 000 elements defined on $\mathbf{B} = [-8x_0, 8x_0] \times [-8x_0 2\pi f_d, 8x_0 2\pi f_d] \times [-2, 2]$ is sufficient to obtain all the existing orbits for f_d. Note that the size of $\mathbf{B}$ varies with the vibration frequency. The numerical solution of the equation system (2) is obtained by explicit integration with a Dormand-Prince method [39]. For each IC, the calculation is carried out until convergence to a periodic orbit is reached, within the limit of 10 000 periods. In the absence of convergence, the solution is considered chaotic. A dedicated Python and Nvidia-CUDA code is written for this task and executed on an NVIDIA RTX A5000 GPU with 8 192 CUDA cores. A representative grid of ICs $\mathbf{X}(0) = \begin{pmatrix} x(0) & \dot{x}(0) & v(0) \end{pmatrix}^\top$ with 8 000 points is defined for all vibration frequencies. For each frequency between 10 and 80 Hz, a simulation is performed from each $\mathbf{X}(0)$ until convergence to a periodic or chaotic regime is reached. The whole calculation took 8 minutes with GPU. The stable orbits are deduced and classified by type (harmonic or chaotic) and, if necessary, by subharmonic, i.e., those for which the mass oscillates at a frequency which is a submultiple of the vibration frequency. An orbit is called *high* when it crosses the saddle point ($x = 0$) and goes from one stable equilibrium to the other. It is considered *low* when it oscillates around one of the two stable equilibrium points $\pm x_0$. Throughout the present article, we will use the following notations: H1H (resp. H1L) for first order high (resp. low) harmonic orbit and SH3H (resp. SH3L) for third order high (resp. low) subharmonic orbit. Therefore, SH*kJ* denotes a subharmonic of order $k \in \mathbb{N}_1 \setminus \{1\}$ and height $J = H$ or L. We arbitrarily choose that Chaos is of order 0. The subset corresponding to the ICs that leads to orbits of order $k \in \mathbb{N}_0$ is noted O_k. Moreover, these are partitioned by those that lead to high H_k and those that lead to low L_k orbits, i.e., $O_k = H_k \sqcup L_k$ and $\mathbf{G} = \bigsqcup_k O_k$. In the particular case of Chaos, the ICs subset is noted as O_0. Figures 6 and 7 show the harvester dynamics in the $(x/x_0, \dot{x}/x_0\omega_0)$ plane for $f_d = 25$ Hz and $f_d = 50$ Hz, respectively. Figure 6 depicts Chaos (salmon curves) as well as H1H (dark blue closed curve), while Fig. 7 depicts H1H (dark
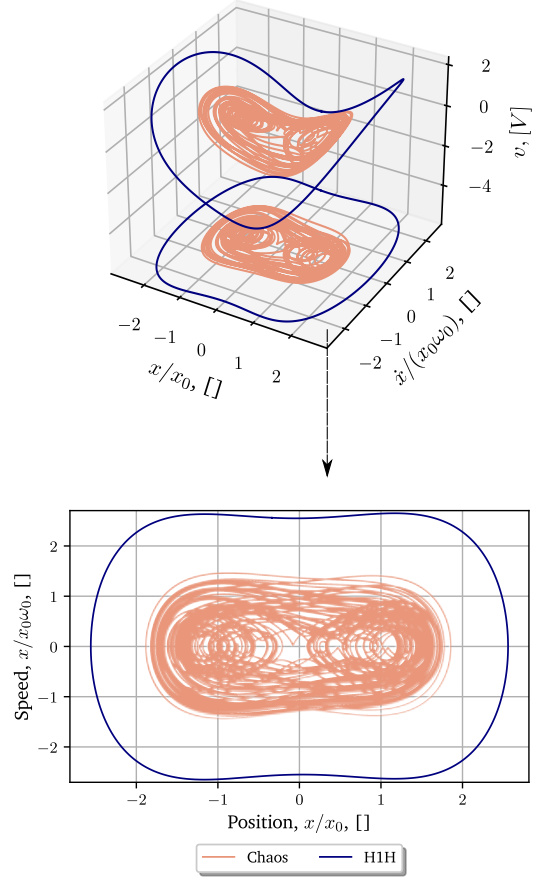

Fig. 6: 3D phase plane $(x/x_0, \dot{x}/x_0\omega_0, v)$ and orbit projection in the 2D plane $(x/x_0, \dot{x}/x_0\omega_0)$ for $f_d = 25$ Hz.

blue), H1L (light blue), SH3L (light orange), SH3H (dark orange), and SH5H (dark pink) in the state space. As proved by Fig. 6 and 7, various orbits exhibiting different harvested power can exist for a given excitation.

3. Power expectation

In this section, the harvested power and the probability of occurrence associated with each orbit are studied. From these quantities, a new metric named the power expectation is introduced and is applied to quantitatively evaluate NVEH performance.

3.1. Power associated with a given orbit

The average harvested power corresponds to the power dissipated in the resistor R connected to the piezoelectric
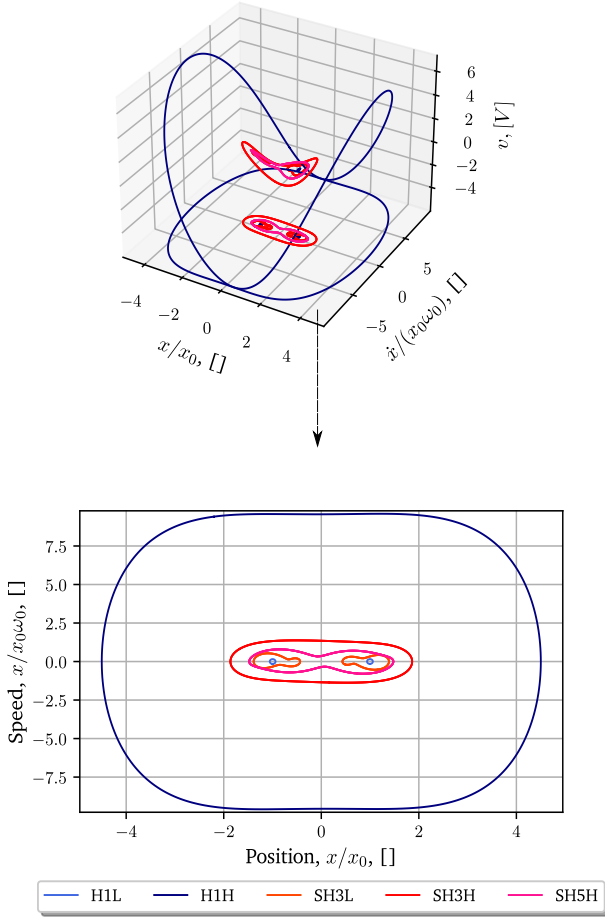
orbit for $f_d = 25$ Hz and $f_d = 50$ Hz. We can see that the power of high orbits are logically more important than those of low orbits. Figure 8 shows the power of all existing orbits for vibration frequencies between 10 Hz and 80 Hz. One may note that both the power and the existence of each orbit vary with the vibration frequency. The high (resp. low) orbits see their energy increase (resp. decrease) with the vibration frequency. For example, the H1H (resp. H1L) orbit sees its power increase (resp. decrease) by a factor 100 from 10 Hz to 67 Hz (resp. 27 Hz to 80 Hz). The H1H is the orbit maximizing the harvested power, but no longer exists from 67 Hz, called *cutoff frequency* of H1H in the following. The two H1L (around $-x_0$ and x_0) are the less interesting orbits and persist until they are the only existing orbits above 80 Hz.

Fig. 7: 3D phase plane $(x/x_0, \dot{x}/x_0\omega_0, v)$ and orbit projection in the 2D plane $(x/x_0, \dot{x}/x_0\omega_0)$ for $f_d = 50$ Hz.

	ICs	P_h at 25 Hz [mW]	P_h at 50 Hz [mW]
H1L	O_1		$3.29.10^{-4}$
H1H	O_1	0.24	2.63
SH3L	O_3		$7.52.10^{-3}$
SH3H	O_3		$5.98.10^{-2}$
SH5H	O_5		$1.77.10^{-2}$
Chaos	O_0	$2.03.10^{-2}$	

Table 3: ICs subsets leading to existing orbits and average harvested power associated to each existing orbit for $f_d = 25$ Hz and $f_d = 50$ Hz, respectively.

electrodes and can be computed by the mean value of v^2/R as in (7) or (8).

$$P_h(\text{SH}kJ) = \frac{1}{kT_d} \int_0^{kT_d} \frac{v^2(t)}{R} dt, \quad \text{where } k \in \mathbb{N}_1 \qquad (7)$$

$$P_h(\text{Chaos}) = \frac{1}{nT_d} \int_0^{nT_d} \frac{v^2(t)}{R} dt \quad \text{with } n = 5\,000 \qquad (8)$$

Where T_d corresponds to the ambient vibration period. Here, we consider the previously defined grid $\boldsymbol{G}$ (6) as the ICs set so that all existing orbits are detected for each vibration frequency. A numerical simulation is performed from each IC $\boldsymbol{X}(0) \in \boldsymbol{G}$ until we stabilize on a given orbit of order $k \in \mathbb{N}_0$. For all order k, an average power can be associated with each orbit. Table 3 shows the average power P_h for each existing

3.2. Probability associated with a given orbit

To provide a fair evaluation of a given harvester and for all vibration frequencies, we define a probability of occurrence r for each existing high (resp. low) k-orbit that corresponds to the ratio of the cardinality of ICs H_k (resp. L_k) and the cardinality of the grid of ICs considered $\boldsymbol{G}$ (number of elements of $\boldsymbol{G}$ that is $|\boldsymbol{G}| = |I|$). For orbits of order 1, this means:

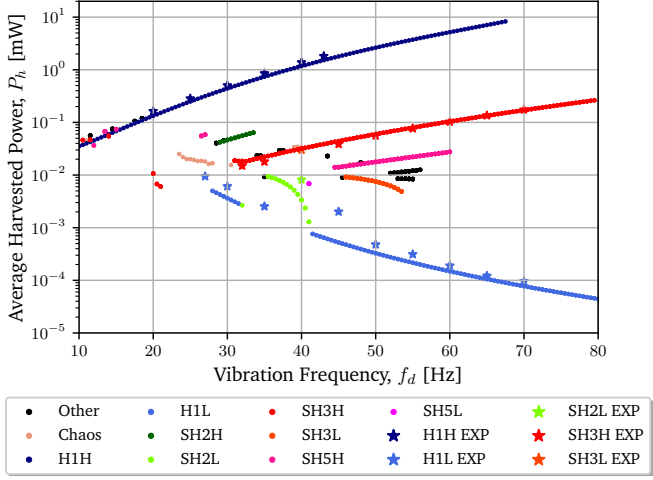$$r(\text{H1H}) = \frac{|H_1|}{|\boldsymbol{G}|} \qquad r(\text{H1L}) = \frac{|L_1|}{|\boldsymbol{G}|} \qquad (9)$$

Fig. 8: Orbital average harvested power P_h obtained numerically (points) and experimentally (stars) as a function of the vibration frequency f_d for a constant amplitude $A = 2.5$ m.s^{-2}.

For orbits of order $k \in \mathbb{N}_1 \setminus \{1\}$ (subharmonic):

$$r(\mathrm{SH}k\mathrm{H}) = \frac{|H_k|}{|\boldsymbol{G}|} \qquad r(\mathrm{SH}k\mathrm{L}) = \frac{|L_k|}{|\boldsymbol{G}|} \qquad (10)$$

In the particular case of Chaos, $r(\mathrm{Chaos}) = |O_0|/|\boldsymbol{G}|$. For example, with an ICs grid of 8 000 starting points at 50 Hz, 3 488 converged to an H1L, i.e., $|L_1| = 3\,488$ and so $r(\mathrm{H1L}) = 3\,488/8\,000 = 43.6\%$. Figure 9 shows the ICs $(x/x_0, \dot{x}/x_0\omega_0)$ that converge toward H1H (in dark blue), the ICs that converge toward H1L (in light blue), and the ICs that converge toward SH3H (in red). In order to enhance the visualization of each orbit's basin of attraction, 400 000 ICs are computed. Table 4 summarizes the probabilities of occurrence of each existing orbit when the vibration frequency is 50 Hz. For this vibration frequency, the system tends to converge toward the lowest orbit, i.e., H1L, because it exhibits the highest probability. Note that the probability of occur-

	H1L	H1H	SH3L	SH3H	SH5H
r [%]	43.6	16.1	10.3	23.0	7.0

Table 4: Probabilities of occurrence for each orbit for $f_d = 50$ Hz with a starting points grid of 8 000 elements.

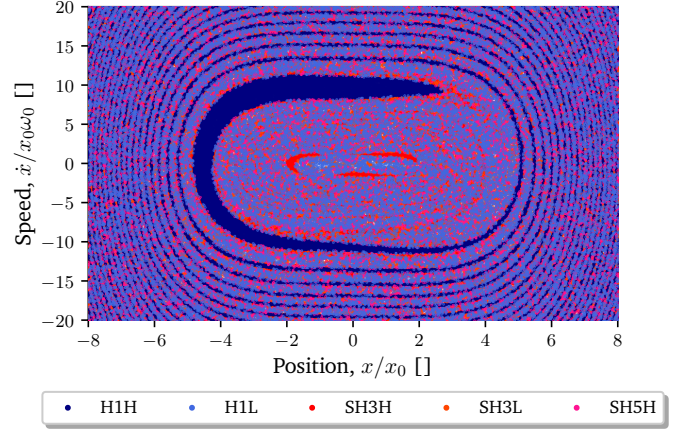rence of each orbit can be modified by selecting a relevant

Fig. 9: Basins of attraction for $f_d = 50$ Hz with a grid of 400 000 starting points.

subset of the ICs grid $\boldsymbol{G}$. In the following sections, this will be defined as an orbit jump strategy, as described in section 3.4 and in Fig. 10.

3.3. Definition of the power expectation

By means of the harvested power P_h and the probability of occurrence r that are associated with each existing orbit at each vibration frequency, we can compute *the power expectation* – noted $\overline{P}$ – of the ICs grid. The power expectation is defined as the sum of the average harvested power pondered by the probability of occurrence associated with each orbit as in (11). We note $N \in \mathbb{N}_1 \setminus \{1\}$ the maximum order of existing orbits.

$$\overline{P}[rP_h](f_d) = (rP_h)(\mathrm{Chaos}) + (rP_h)(\mathrm{H1H}) + (rP_h)(\mathrm{H1L})$$
$$+ \sum_{2 \leq k \leq N, J = H, L} (rP_h)(\mathrm{SH}k\mathrm{J})$$

$$(11)$$

The power expectation can be used to quantify the statistical power of a VEH according to its probabilities of converging to the existing orbits. The power expectation strongly depends on the ICs grid used in simulation. This means that some ICs grids will lead to low power expectations, while some other ICs grids lead to large power expectations. Therefore, an orbit jump strategy – such as [5] or [22] – can be interpreted as

a change of the ICs grid in order to increase the probability of high-energy orbits. The next section aims at exploring the power expectation of NVEH with three ICs grids corresponding to three fictive orbit jump strategies.

3.4. Application of the power expectation to three sets of ICs

Consider three initial grids G, G^L and G^H where G^L and G^H are two subsets of G. These grids represent three theoretical orbit jump strategies for a vibration frequency equal to 50 Hz. We denote "random strategy" the orbit jump strategy associated with G, "minimum strategy"[1] the orbit jump strategy associated with G^L and "maximum strategy"[2] the orbit jump strategy associated with G^H. The random strategy consists in starting at initial states belonging to the uniformly distributed initial grid G that is previously defined in (6). With such an ICs grid, the system converges to a wide range of orbits. Table 4 shows the probability of occurrence of each existing orbit for this random strategy for $f_d = 50$ Hz. The minimum strategy always leads to the lowest existing orbit which is the H1L at 50 Hz. The corresponding grid G^L is the subset of G that leads to the orbits H1L at 50 Hz. Thus, it corresponds to the worst case for the NVEH. The maximum strategy consists in always reaching the highest existing orbit which corresponds to H1H for 50 Hz. The corresponding grid G^H is the subset of G that leads to the H1H for 50 Hz. Table 5 gives the probabilities r, the average harvested power of each orbit P_h, and the power expectation for the three ICs grids for a vibration frequency $f_d = 50$ Hz. The power expectation of the random strategy $\overline{P}$ lies between the power expectations of the minimum $\overline{P}^L$ and the maximum $\overline{P}^H$ strategies which constitute the lower and upper bounds of the power expectation. Figure 10 shows the probability of occurrence r of each orbit for every vibration frequency between 10 and 80 Hz for the three aforementioned sets of ICs. Note that "Other" gathers
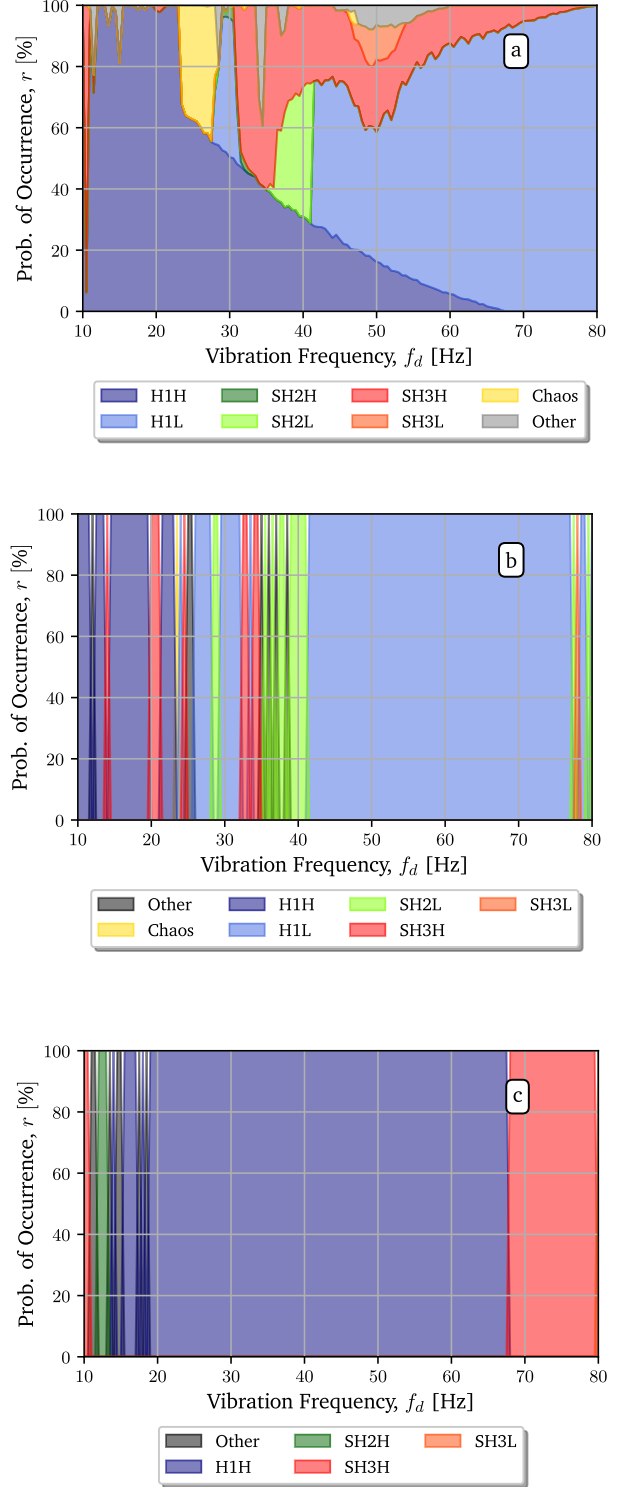
---

[1]Note that the minimum strategy is defined in order to quantify the minimum power that can be harvested with a bistable NVEH.

[2]Note that the maximum strategy is a theoretical orbit jump strategy that makes it possible to evaluate the maximum power that can be harvested with a bistable NVEH but remains challenging to implement.

Fig. 10: Probability of occurrence r of each existing orbit as a function of the vibration frequency f_d for (a) the random strategy, (b) the minimum strategy, and (c) the maximum strategy. The denomination "Other" regroups all the orbits not indicated in the legend.

the summed probabilities of all the orbits that are not indicated in the legend of Fig. 10. Figure 10(a) shows that for a
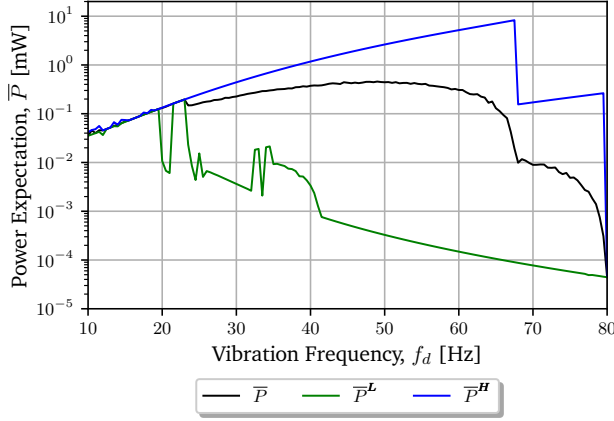
Fig. 11: Power expectation curves associated to the three strategies with $f_d \in [10\,\mathrm{Hz}, 80\,\mathrm{Hz}]$.

	G	G^L	G^H	$P_h\,[\mathrm{mW}]$
$r(\mathrm{H1L})$	43.6	100	0	$3.29.10^{-4}$
$r(\mathrm{H1H})$	16.1	0	100	2.63
$r(\mathrm{SH3L})$	10.3	0	0	$7.52.10^{-3}$
$r(\mathrm{SH3H})$	23.0	0	0	$5.98.10^{-2}$
$r(\mathrm{SH5H})$	7.0	0	0	$1.77.10^{-2}$
$\overline{P}\,[\mathrm{mW}]$	0.44	$3.29.10^{-4}$	2.63	

Table 5: Probabilities and average harvested power for each orbit and power expectation for the three sets of ICs for $f_d = 50$ Hz.

vibration frequency of 25 Hz, the non-zero probabilities are those of H1L and Chaos which is confirmed by the transient analysis shown in Fig. 6. Figure 10(b,c) illustrates that for most vibration frequencies, the power expectation of the minimum strategy corresponds to the harvested power with the H1L. Furthermore, for most vibration frequencies, the power expectation of the maximum strategy corresponds to the harvested power with the H1H. Figure 11 shows the power expectation curves associated with each proposed orbit jump strategy for all vibration frequencies. Interestingly, the power expectation of the random strategy exhibits a quasi-plateau on a large range of frequencies, between 20 Hz to 65 Hz, which reveals the broadband nature of the NVEH. Figure 11 also shows that the minimum and maximum strategies ex-

hibit the same power expectation around 20 Hz, meaning that there is little to no gain in implementing an orbit jump strategy for $f_d = 20$ Hz. On the other hand, for $f_d = 60$ Hz, the power expectation with the maximum strategy is 30 000 times larger than the one with the minimum strategy. Therefore, the power brought by an effective orbit jump strategy might be relatively important, around 60 Hz.

The power expectation enables the evaluation of the influence of VEH characteristics, excitation nature, and the orbit jump strategy on the performances of the NVEH (for a given vibration frequency and level of excitation).

4. Performance assessment with the power expectation

In this section, we define $\mathrm{FoM}_{\overline{P}}$ based on the aforementioned power expectation. Such an FoM makes it possible to quantitatively evaluate a given bistable energy harvester associated with a given orbit jump strategy. $\mathrm{FoM}_{\overline{P}}$ is then studied as a function of the acceleration amplitude to quantitatively illustrate the dependence of bistable VEH performance on the excitation level.

4.1. Linear equivalent model

The linear equivalent model is a candidate for comparison with the considered NVEH. To define the linear equivalent model of NVEH, small displacements of the mass around one of its equilibrium stable positions when $x = x_0$ (given in section 2) are considered. A first order linearization of the equation system (2) is applied, with $x = x_0 + \delta x$ and $\delta x << x_0$. The corresponding equations are given by (12). We choose to take the constant value resistance $R = 1/C_p \omega_0$ that corresponds to the optimal resistance of the linear equivalent for a weakly coupled energy harvester [40, 41].

$$
\begin{cases}
\ddot{\delta x} = -\omega_0^2 \delta x - \dfrac{\omega_0}{Q}\dot{\delta x} - 2\dfrac{\alpha}{ML}x_0\delta v + A\sin(2\pi f_d t) \\[2mm]
\dot{\delta v} = 2\dfrac{\alpha}{LC_0}x_0\dot{\delta x} - \dfrac{1}{RC_0}\delta v
\end{cases}
\tag{12}
$$

The power expectation of the linear equivalent harvester is noted $\overline{P}^{\text{Linear Model}}$. Figure 12 shows $\overline{P}^{\text{Linear Model}}$ (in orange)

10

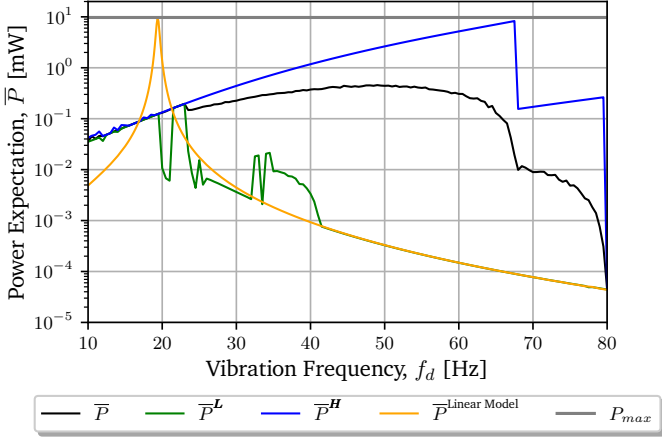as a function of the vibration frequency. The analytical ex-

Fig. 12: Power expectation curves associated with the three aforementioned orbit jump strategies and the linear equivalent with an acceleration amplitude $A = 2.5$ m.s^{-2}. The horizontal line (in gray) illustrates the power limit of the NVEH model given in (13).

pression of the maximum power that can be harvested with such a system is known [42] and given in equation (13).

$$P_{max} = \frac{MA^2Q}{8\omega_0} \qquad (13)$$

With our PEH – whose characteristics are summarized in Table 2 – the maximum power is given by $P_{max} \simeq 9.7$ mW. The maximum power with the NVEH and linear equivalent are the same[3] [45] and are reached when the vibration frequency matches the cutoff frequency of H1H (for the NVEH) or the resonant frequency (for the linear equivalent). Figure 12 shows that the power expectation with the random strategy is higher than the power expectation of the linear equivalent over a wide range of vibration frequencies, between 25 and 80 Hz. Over this frequency range, the power expectation is even larger with the maximum strategy.

4.2. Definition of an expectation-based FoM

FoM$_{\overline{P}}$ (14) consists in the integral of the power expectation $\overline{P}$ divided by the integral of the linear equivalent power expectation $\overline{P}^{\text{Linear Model}}$ over the considered frequency interval.

---

[3]The power limit of a linear and a nonlinear energy harvester are identical [43, 44].

$$\text{FoM}_{\overline{P}} = \int_{f_d} \overline{P}(f)\,df \,/\, \int_{f_d} \overline{P}^{\text{Linear Model}}(f)\,df \qquad (14)$$

FoM$_{\overline{P}}$ makes it possible to compare the performance of the NVEH for a given orbit jump strategy. Thus, for a given NVEH, an FoM$_{\overline{P}}$ value can be computed for any orbit jump strategy. The results for the NVEH considered and the three orbit jump strategies defined in section 3.4 are given in Table 6. FoM$_{\overline{P}}$ of the random and maximum strategies are larger

	G	G^L	G^H
FoM$_{\overline{P}}$	2.02	0.16	16.46

Table 6: FoM$_{\overline{P}}$ value for the three sets of ICs associated with the three aforementioned strategies.

than 1, but the FoM$_{\overline{P}}$ of the minimum strategy is much lower than 1. Therefore, with the random and maximum strategies (resp. minimum strategy), the NVEH performances are higher (resp. is lower) than the linear equivalent performances. It is therefore crucial to implement an efficient orbit jump strategy when using an NVEH.

4.3. Evolution of the FoM$_{\overline{P}}$ with the acceleration amplitude

In this section, we study the evolution of the aforementioned FoM$_{\overline{P}}$ and power expectation as a function of the acceleration amplitude A. For this purpose, we study four acceleration amplitudes $A_1 = 1.25$ m.s^{-2}, $A_2 = 2.5$ m.s^{-2}, $A_3 = 5$ m.s^{-2} and $A_4 = 10$ m.s^{-2}. Figure 13 shows the power expectation for each of the three orbit jump strategies and the limit power (13) that can be harvested for each acceleration amplitude. The power expectation curves of the minimum (dotted lines) and random (solid lines) strategies appear noisy, i.e., around 20-25 Hz. Indeed, for this frequency range, many behaviors coexist, such as SH5L, SH3H, or Chaos. The simulations are run over a wider frequency range because the cutoff frequency of the H1H increases with the acceleration amplitude. For instance, this cutoff frequency is around 137 Hz for $A_4 = 10$ m.s^{-2} while it is below 50 Hz for $A_1 = 1.25$ m.s^{-2}. Moreover, it is necessary to define a larger
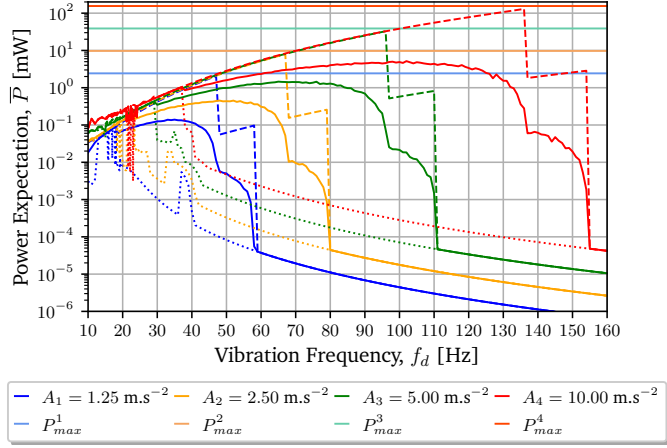
Fig. 13: Power expectation curves for the random strategy (solid lines), for the minimum strategy (dotted lines) and for the maximum strategy (dashed lines) associated with the four amplitudes. The horizontal lines illustrate the power limits (described by (13)) of the NVEH model associated with each acceleration amplitude.

	G	G^L	G^H
A_1	1.86	0.22	12.86
A_2	2.05	0.16	16.45
A_3	2.37	0.14	22.63
A_4	2.71	0.09	30.50

Table 7: $\text{FoM}_{\overline{P}}$ value with each orbit jump strategy – random, minimum, maximum – for the four acceleration amplitudes $A_1 = 1.25$ m.s^{-2}, $A_2 = 2.5$ m.s^{-2}, $A_3 = 5$ m.s^{-2} and $A_4 = 10$ m.s^{-2}.
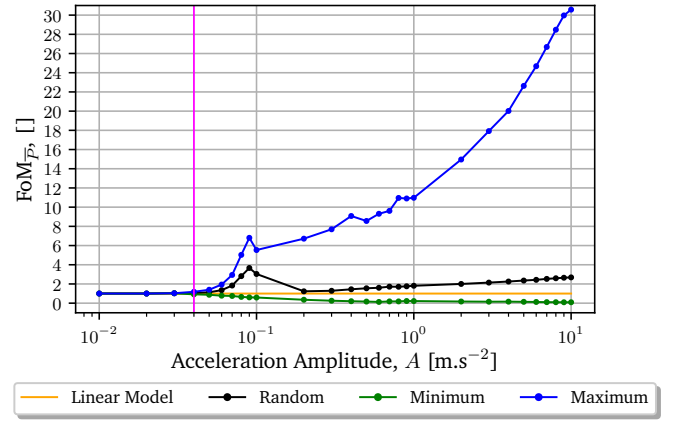

Fig. 14: $\text{FoM}_{\overline{P}}$ for the three orbit jump strategies and $\text{FoM}_{\overline{P}}$'s linear equivalent as a function of the acceleration amplitude A between 0.01 m.s^{-2} and 10 m.s^{-2}. The vertical magenta line corresponds to the acceleration amplitude where the FoM strategies differ in more than 10 %.

ICs grid (in the case where the amplitude A is larger) to detect the H1H until its cutoff frequency. The grid is defined as $\boldsymbol{B} = [-12x_0, 12x_0] \times [-12x_0 2\pi f_d, 12x_0 2\pi f_d] \times [-2, 2]$. As shown in Fig. 13, for low vibration frequencies, the power expectation curves of the maximum strategy do not vary much with the acceleration amplitude. Indeed, the H1H power remains almost identical for any acceleration amplitude. Note that, the acceleration amplitude does not greatly impact the power of the other high orbits such as SH3H. Table 7 summarizes the FoMs for the tested acceleration amplitudes with the three ICs grids. The $\text{FoM}_{\overline{P}}$ is always greater than 1 when the NVEH operates with the random (solid lines) and maximum (dashed lines) strategies under the four acceleration amplitudes. The $\text{FoM}_{\overline{P}}$ of these two strategies increases with acceleration amplitude and growth rate depending on the efficiency of the implemented orbit jump strategy. Table 7 illustrates that the higher the acceleration amplitude, the higher the power expectation with the maximum and random strategies.

Figure 14 shows the evolution of the $\text{FoM}_{\overline{P}}$ for acceleration amplitudes between 0.01 m.s^{-2} and 10 m.s^{-2}. For very small accelerations around $A = 0.01$ m.s^{-2}, the three strategies exhibit an $\text{FoM}_{\overline{P}}$ equal to 1. Indeed, under such small accelera-

tion amplitude, the NVEH behaves like its linearized model, meaning that the performance of the NVEH is the same as the linear equivalent harvester. For an amplitude between 0.01 and 0.03 m.s^{-2}, the three strategies show identical $\text{FoM}_{\overline{P}}$ because the only existing orbit is H1L. For acceleration amplitudes between 0.04 and 0.1 m.s^{-2}, the NVEH (with any orbit jump strategy) exhibits monostable softening nonlinearities (intra-well motions). For this range of acceleration amplitudes, the $\text{FoM}_{\overline{P}}$ of the NVEH is greater than the $\text{FoM}_{\overline{P}}$ of the linear equivalent harvester with the random and maximum strategies. For larger acceleration amplitudes, the $\text{FoM}_{\overline{P}}$ of the minimum strategy keeps on decreasing while the $\text{FoM}_{\overline{P}}$ of the random and maximum strategies always increase along with the acceleration amplitude. Note that when the random strategy is implemented, the NVEH performances are always

better than the performances of the linear equivalent. This proves that bistable energy harvesters, even with a "random" orbit jump strategy, can still outperform linear energy harvesters for a large range of acceleration amplitudes. On the other hand, if the NVEH always stays in its lowest existing orbit (minimum strategy), NVEH performance is much lower than the performance of the linear equivalent harvester. As shown in Fig. 14, the $\text{FoM}_{\overline{P}}$ gain brought by the maximum strategy (compared to the two other strategies) increases with the acceleration amplitude. Figure 14 proves that implementing an orbit jump strategy becomes more crucial as acceleration is increased. As a matter of example, there is little to no gain in finding the best orbit jump strategy if the acceleration is very small (around 0.01 m.s^{-2}), since all the strategies $\text{FoM}_{\overline{P}}$ are around 1. However, for an acceleration amplitude of 2 m.s^{-2}, a good (blue curve) orbit jump strategy makes it possible to multiply the $\text{FoM}_{\overline{P}}$ by about 87 compared to a bad (green curve) orbit jump strategy. Therefore, the $\text{FoM}_{\overline{P}}$ also evaluates the potential efficiency of an orbit jump strategy and makes it possible to determine the most efficient range of acceleration amplitude for such an orbit jump strategy. The influences of other parameters (e.g., resistance of the load, electromechanical coupling) of the bistable VEH are investigated and detailed in Appendix A.

5. Application of the proposed metrics to evaluate an orbit jump strategy in the literature

This section presents the application of the $\text{FoM}_{\overline{P}}$ to the orbit jump strategy presented in [24]. The proposed orbit jump strategy is experimentally validated in [24], and makes it possible to jump from low orbits to high orbits by injecting energy in the mass by tuning the buckling level at the right instants. Specifically, this method is based on a transient increase of the buckling level, i.e., an increase of the stable position x_0 by a factor k_{x_0} between two instants t_0 and t_1. In the proposed method, the jump duration is deliberately short so that $t_1 - t_0 \leq T_d$. For each vibration frequency f_d, the IC corresponding to the lowest possible orbit is used. In

the simulations, the following set of parameters is explored, which correspond to realistic values [24]:

- $t_0 \in [0, t_1]$

- $t_1 \in [0.1T_d, 2.1T_d]$

- $k_{x_0} \in [0.5, 3]$

Simulations are run with each combination of t_0, t_1 and k_{x_0}. In order to evaluate the invested energy during the orbit jump, E_{invest} is computed as follows:

$$E_{\text{invest}} = E_p(x_0^+) - E_p(x_0^-) + E_p(x_1^+) - E_p(x_1^-) \qquad (15)$$

$$= \Delta E_1 + \Delta E_2 \qquad (16)$$

where $x_i^{\pm} = x(t_i^{\pm}) = x(t_i \pm \Delta t)$, for $i = 0, 1$ with Δt the numerical time step. The expression of the potential energy $E_p(\cdot)$ is given in (3). ΔE_1 corresponds to the invested energy when the stable position is modified from x_0 to $k_{x_0}x_0$, and ΔE_2 is the invested energy when the stable position is tuned from $k_{x_0}x_0$ to x_0. In order to find the optimal set of parameters $(t_0, t_1, k_{x_0})_{\text{opt}}$, the parameters leading to the highest orbit are determined. Among these parameters, the optimal set that minimizes invested energy E_{invest} is selected for each vibration frequency. Finally, in order to take into account the experimental variability of the set parameters, we compute the probability of reaching each orbit when the optimal parameters vary uniformly from -5 % to +5 % for t_0 and t_1 and from 0 % to +10 % for k_{x_0}. These probabilities make it possible to compute the power expectation of the proposed orbit jump strategy as a function of the vibration frequency, f_d.

Figure 15 shows that the proposed orbit jump is particularly efficient for frequencies between [25 Hz, 49 Hz]. Indeed, Fig. 15(a) shows that its power expectation (in purple) is close to the maximum strategy on this frequency range. However, for larger vibration frequencies, we can observe that the power expectation of the proposed orbit jump drops. Indeed, the orbit jump strategy does not make it possible to jump to H1H when $f_d > 49$ Hz because the energy gap between H1H and H1L becomes too large. Figure 15(b) shows
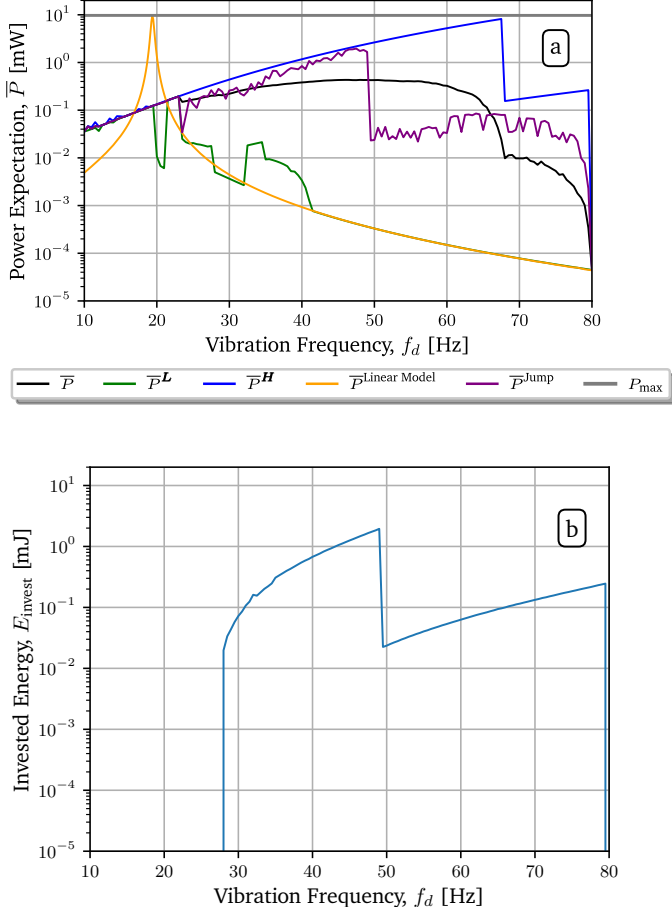
Fig. 15: (a) Power expectation curves associated with the three aforementioned orbit jump strategies, the linear equivalent and the investigated orbit jump strategy inspired from [24], as a function of f_d, with simulated experimental variation. The horizontal line (in gray) illustrates the power limit of the NVEH model given in (13). (b) Invested energy for performing the orbit jump as a function of the vibration frequency f_d.

the invested energy for the studied orbit jump strategy. The invested energy increases with the vibration frequency, because the energy gap between H1L and H1H gets larger with higher frequencies. When the vibration frequency reaches 49 Hz, the invested energy drops because the H1H cannot be reached and the SH3H becomes the targeted orbit for the jump. Similarly, the invested energy drops around 78 Hz because the SH3H cannot be reached with the investigated orbit jump strategy. Note that the maximum value of the invested energy remains below 2 mJ, which remains reasonable considering the harvested power while in H1H.

The FoM$_{\overline{P}}$ of the bistable PEH with the investigated orbit jump strategy is equal to 2.9. This is 17 times larger than the minimum strategy FoM$_{\overline{P}}$, which demonstrates the effec-

tiveness of the orbit jump strategy inspired from [24]. However, the investigated orbit jump strategy FoM$_{\overline{P}}$ is also 6 times lower than the maximum strategy, which proves that there is still room for finding better orbit jump approaches. Note that the FoM$_{\overline{P}}$ corresponding to the investigated orbit jump strategy is 2.9 times larger than 1, meaning that the bistable VEH implementing this orbit jump strategy is 2.9 times better than the linear equivalent VEH.

6. Conclusion and perspectives

In this paper, we defined a metric – called power expectation – that takes into account existing subharmonic behaviors using the average harvested power and the probability of occurrence of each existing orbit for a vibration frequency set. We observed that the power expectation value depends on the harvester type and the potential orbit jump strategy implemented. Thereafter, we defined FoM$_{\overline{P}}$ – based on the power expectation – to analyze the performances of an NVEH with a given orbit jump strategy. The FoM$_{\overline{P}}$ makes it possible to quantitatively assess the effectiveness of orbit jump strategies by comparing the performance of an NVEH to its linear equivalent harvester. The influence of the acceleration amplitude on the performances of the NVEH is also discussed, based on FoM$_{\overline{P}}$. Finally, the proposed metrics are applied to evaluate the performance of an orbit jump strategy from the literature. This analysis proves that the proposed metrics are a promising tool to assess the performance of a given orbit jump strategy associated with a PEH. In future works, the FoM$_{\overline{P}}$ will be used to define the best NVEH parameters for a given acceleration amplitude. It will also be used to assess and compare various orbit jump strategies and to quantify their performance uniformly.

7. Conflict of interest

The authors declare no competing financial interest.

References

[1] N. Sezer, M. Koç, A comprehensive review on the state-of-the-art of piezoelectric energy harvesting, Nano Energy 80 (2021) 105567. `doi:10.1016/j.nanoen.2020.105567`.

[2] E. Halvorsen, Energy Harvesters Driven by Broadband Random Vibrations, Journal of Microelectromechanical Systems 17 (5) (2008) 1061–1071. `doi:10.1109/JMEMS.2008.928709`.

[3] L.-C. J. Blystad, E. Halvorsen, S. Husa, Piezoelectric MEMS energy harvesting systems driven by harmonic and random vibrations, IEEE Transactions on Ultrasonics, Ferroelectrics and Frequency Control 57 (4) (2010) 908–919. `doi:10.1109/TUFFC.2010.1495`.

[4] F. Cottone, H. Vocca, L. Gammaitoni, Nonlinear energy harvesting, Physical review letters 102 (8) (2009) 080601. `doi:10.1103/PhysRevLett.102.080601`.

[5] G. Sebald, H. Kuwano, D. Guyomar, B. Ducharne, Simulation of a Duffing oscillator for broadband piezoelectric energy harvesting, Smart Materials and Structures 20 (7) (2011) 075022. `doi:10.1088/0964-1726/20/7/075022`.

[6] T. Huguet, A. Badel, M. Lallart, Exploiting bistable oscillator subharmonics for magnified broadband vibration energy harvesting, Applied Physics Letters 111 (17) (2017) 173905. `doi:10.1063/1.5001267`.

[7] T. Huguet, A. Badel, O. Druet, M. Lallart, Subharmonic orbits and their stability robustness to greatly enhance the bandwidth of bistable vibration energy harvesters, in: T. E. Matikas (Ed.), Smart Materials and Nondestructive Evaluation for Energy Systems IV, Vol. 10601, International Society for Optics and Photonics, SPIE, 2018, pp. 66 – 77. `doi:10.1117/12.2287827`.

[8] R. Kumar, S. Gupta, S. F. Ali, Energy harvesting from chaos in base excited double pendulum, Mechanical Systems and Signal Processing 124 (2019) 49–64. `doi:10.1016/j.ymssp.2019.01.037`.

[9] A. Erturk, D. Inman, Broadband piezoelectric power generation on high-energy orbits of the bistable Duffing oscillator with electromechanical coupling, Journal of Sound and Vibration 330 (10) (2011) 2339–2353. `doi:10.1016/j.jsv.2010.11.018`.

[10] R. L. Harne, K. W. Wang, A review of the recent research on vibration energy harvesting via bistable systems, Smart Materials and Structures 22 (2) (2013) 023001. `doi:10.1088/0964-1726/22/2/023001`.

[11] S. Fang, S. Zhou, D. Yurchenko, T. Yang, W.-H. Liao, Multistability phenomenon in signal processing, energy harvesting, composite structures, and metamaterials: A review, Mechanical Systems and Signal Processing 166 (2022) 108419. `doi:10.1016/j.ymssp.2021.108419`.

[12] Y. Jia, Review of nonlinear vibration energy harvesting: Duffing, bistability, parametric, stochastic and others, Journal of Intelligent Material Systems and Structures 31 (7) (2020) 921–944. `doi:10.1177/1045389X20905989`.

[13] X. Ma, H. Li, S. Zhou, Z. Yang, G. Litak, Characterizing nonlinear characteristics of asymmetric tristable energy harvesters, Mechanical Systems and Signal Processing 168 (2022) 108612. `doi:10.1016/j.ymssp.2021.108612`.

[14] G. Litak, M. I. Friswell, S. Adhikari, Magnetopiezoelastic energy harvesting driven by random excitations, Applied Physics Letters 96 (21) (2010) 214103. `doi:10.1063/1.3436553`.

[15] S.-J. Jang, I.-H. Kim, K. Park, H.-J. Jung, An enhanced tunable rotational energy harvester with variable stiffness system for low-frequency vibration, Proceedings of the Institution of Mechanical Engineers, Part C: Journal of Mechanical Engineering Science 230 (5) (2016) 732–736. `doi:10.1177/0954406215587727`.

[16] H. Liu, H. Fu, L. Sun, C. Lee, E. M. Yeatman, Hybrid energy harvesting technology: From materials, structural design, system integration to applications, Renewable and Sustainable Energy Reviews 137 (2021) 110473. `doi:10.1016/j.rser.2020.110473`.

[17] L.-C. Zhao, H.-X. Zou, Z.-Y. Wu, Q.-H. Gao, G. Yan, F.-R. Liu, K.-X. Wei, W.-M. Zhang, Dynamically synergistic regulation mechanism for rotation energy harvesting, Mechanical Systems and Signal Processing 169 (2022) 108637. `doi:10.1016/j.ymssp.2021.108637`.

[18] V. N. Pilipchuk, A. F. Vakakis, M. A. F. Azeez, Sensitive Dependence on Initial Conditions of Strongly Nonlinear Periodic Orbits of the Forced Pendulum, Nonlinear Dynamics 16 (3) (1998) 223–237. `doi:10.1023/A:1008276310599`.

[19] H. Bao, N. Wang, B. Bao, M. Chen, P. Jin, G. Wang, Initial condition-dependent dynamics and transient period in memristor-based hypogenetic jerk system with four line equilibria, Communications in Nonlinear Science and Numerical Simulation 57 (2018) 264–275. `doi:10.1016/j.cnsns.2017.10.001`.

[20] D. Mallick, A. Amann, S. Roy, Surfing the High Energy Output Branch of Nonlinear Energy Harvesters, Physical Review Letters 117 (19) (2016) 197701. `doi:10.1103/PhysRevLett.117.197701`.

[21] Y. Huang, Z. Zhao, W. Liu, Systematic adjustment strategy of a nonlinear beam generator for high-energy orbit, Mechanical Systems and Signal Processing 166 (2022) 108444. `doi:10.1016/j.ymssp.2021.108444`.

[22] S. Zhou, J. Cao, D. J. Inman, S. Liu, W. Wang, J. Lin, Impact-induced high-energy orbits of nonlinear energy harvesters, Applied Physics Letters 106 (9) (2015) 093901. `doi:10.1063/1.4913606`.

[23] C. Lan, G. Hu, Y. Liao, W. Qin, A wind-induced negative damping method to achieve high-energy orbit of a nonlinear vibration en-

15

ergy harvester, Smart Materials and Structures 30 (2) 02LT02. `doi:10.1088/1361-665X/abd962`.

[24] T. Huguet, M. Lallart, A. Badel, Orbit jump in bistable energy harvesters through buckling level modification, Mechanical Systems and Signal Processing 128 (2019) 202–215. `doi:10.1016/j.ymssp.2019.03.051`.

[25] Y. Huang, W. Liu, Y. Yuan, Z. Zhang, High-energy orbit attainment of a nonlinear beam generator by adjusting the buckling level, Sensors and Actuators A: Physical 312 (2020) 112164. `doi:10.1016/j.sna.2020.112164`.

[26] J. Wang, W.-H. Liao, Attaining the high-energy orbit of nonlinear energy harvesters by load perturbation, Energy Conversion and Management 192 (2019) 30–36. `doi:10.1016/j.enconman.2019.03.075`.

[27] Y. Zhang, C. Ding, J. Wang, J. Cao, High-energy orbit sliding mode control for nonlinear energy harvesting, Nonlinear Dynamics 105 (1) (2021) 191–211. `doi:10.21203/rs.3.rs-203705/v1`.

[28] A. Badel, E. Lefeuvre, Nonlinear Conditioning Circuits for Piezoelectric Energy Harvesters, in: E. Blokhina, A. El Aroudi, E. Alarcon, D. Galayko (Eds.), Nonlinearity in Energy Harvesting Systems, Springer International Publishing, Cham, 2016, pp. 321–359. `doi:10.1007/978-3-319-20355-3_10`.

[29] Y. Cai, Y. Manoli, A piezoelectric energy-harvesting interface circuit with fully autonomous conjugate impedance matching, 156% extended bandwidth, and 0.38μW power consumption, in: 2018 IEEE International Solid - State Circuits Conference - (ISSCC), 2018, pp. 148–150. `doi:10.1109/ISSCC.2018.8310227`.

[30] A. Morel, Interfaces électriques adaptatives dynamiquement au spectre fréquentiel pour la récupération d'énergie vibratoire large bande, Ph.D. thesis, Université Savoie Mont Blanc (Nov. 2020).
URL `https://hal.archives-ouvertes.fr/tel-03099900`

[31] A. Morel, A. Brenes, D. Gibus, E. Lefeuvre, P. Gasnier, G. Pillonnet, A. Badel, A comparative study of electrical interfaces for tunable piezoelectric vibration energy harvesting, Smart Materials and Structures 31 (4) (2022) 045016. `doi:10.1088/1361-665X/ac54e8`.

[32] T. Huguet, Vers une meilleure exploitation des dispositifs de récupération d'énergie vibratoire bistables: Analyse et utilisation de comportements originaux pour améliorer la bande passante, Ph.D. thesis (2018).
URL `https://tel.archives-ouvertes.fr/tel-01957377`

[33] I. Iliuk, J. M. Balthazar, A. M. Tusset, J. L. P. Felix, B. R. de Pontes, On Non-ideal and Chaotic Energy Harvester Behavior, Differential Equations and Dynamical Systems 21 (1-2) (2013) 93–104. `doi:10.1007/s12591-012-0127-5`.

[34] J. Cao, A. Syta, G. Litak, S. Zhou, D. J. Inman, Y. Chen, Regular and chaotic vibration in a piezoelectric energy harvester with fractional damping, The European Physical Journal Plus 130 (6) (2015) 103. `doi:10.1140/epjp/i2015-15103-8`.

[35] W. Q. Liu, A. Badel, F. Formosa, Y. P. Wu, A new figure of merit for wideband vibration energy harvesters, Smart Materials and Structures 24 (12) (2015) 125012. `doi:10.1088/0964-1726/24/12/125012`.

[36] S. P. Beeby, R. N. Torah, M. J. Tudor, P. Glynne-Jones, T. O'Donnell, C. R. Saha, S. Roy, A micro electromagnetic generator for vibration energy harvesting, Journal of Micromechanics and Microengineering 17 (7) (2007) 1257–1265. `doi:10.1088/0960-1317/17/7/007`.

[37] P. D. Mitcheson, G. K. Rao, T. C. Green, Energy Harvesting From Human and Machine Motion for Wireless Electronic Devices, Proceedings of the IEEE 96 (2008) 1457–1486. `doi:10.1109/JPROC.2008.927494`.

[38] W. Q. Liu, A. Badel, F. Formosa, Y. P. Wu, A. Agbossou, Novel piezoelectric bistable oscillator architecture for wideband vibration energy harvesting, Smart Materials and Structures 22 (3) (2013) 035013. `doi:10.1088/0964-1726/22/3/035013`.

[39] J. Dormand, P. Prince, A family of embedded Runge-Kutta formulae, Journal of Computational and Applied Mathematics 6 (1) (1980) 19–26. `doi:10.1016/0771-050X(80)90013-3`.

[40] Y. Liao, H. A. Sodano, Optimal parameters and power characteristics of piezoelectric energy harvesters with an *RC* circuit, Smart Materials and Structures 18 (4) (2009) 045011. `doi:10.1088/0964-1726/18/4/045011`.

[41] A. Morel, A. Badel, R. Grézaud, P. Gasnier, G. Despesse, G. Pillonnet, Resistive and reactive loads' influences on highly coupled piezoelectric generators for wideband vibrations energy harvesting, Journal of Intelligent Material Systems and Structures 30 (3) (2019) 386–399. `doi:10.1177/1045389X18810802`.

[42] Y. Liao, J. Liang, Maximum power, optimal load, and impedance analysis of piezoelectric vibration energy harvesters, Smart Materials and Structures 27 (7) (2018) 075053. `doi:10.1088/1361-665X/aaca56`.

[43] A. Brenes, A. Morel, J. Juillard, E. Lefeuvre, A. Badel, Maximum power point of piezoelectric energy harvesters: A review of optimality condition for electrical tuning, Smart Materials and Structures 29 (3) (2020) 033001. `doi:10.1088/1361-665X/ab6484`.

[44] C. Lan, Y. Liao, G. Hu, L. Tang, Equivalent impedance and power analysis of monostable piezoelectric energy harvesters, Journal of Intelligent Material Systems and Structures 31 (14) (2020) 1697–1715. `doi:10.1177/1045389X20930080`.

[45] T. Huguet, A. Badel, M. Lallart, Parametric analysis for optimized piezoelectric bistable vibration energy harvesters, Smart Materials and Structures 28 (11) (2019) 115009. `doi:10.1088/1361-665X/ab45c6`.

[46] N. Kawai, Y. Kushino, H. Koizumi, MPPT controled piezoelectric energy harvesting circuit using synchronized switch harvesting on inductor, in: IECON 2015 - 41st Annual Conference of the IEEE Industrial Electronics Society, IEEE, Yokohama, 2015, pp. 001121–001126.

`doi:10.1109/IECON.2015.7392250`.

[47] A. Morel, A. Quelen, C. A. Berlitz, D. Gibus, P. Gasnier, A. Badel, G. Pillonnet, 32.2 Self-Tunable Phase-Shifted SECE Piezoelectric Energy-Harvesting IC with a 30nW MPPT Achieving 446% Energy-Bandwidth Improvement and 94% Efficiency, in: 2020 IEEE International Solid-State Circuits Conference - (ISSCC), IEEE, San Francisco, CA, USA, 2020, pp. 488–490. `doi:10.1109/ISSCC19947.2020.9062972`.

Appendix A. Influence of the resistive load and the electromechanical coupling on the FoM$_{\overline{P}}$

Appendix A.1. Evolution of the FoM$_{\overline{P}}$ with the resistive load

We study the influence of the resistive load on the power expectation and FoM$_{\overline{P}}$. Figure A.16 shows the power expectation curves for $R_1 = 7\,830\,\Omega$, $R_2 = 3\,915\,\Omega$, $R_3 = 1\,957.5\,\Omega$, and $R_4 = 978.75\,\Omega$. When the maximum (resp. ran-
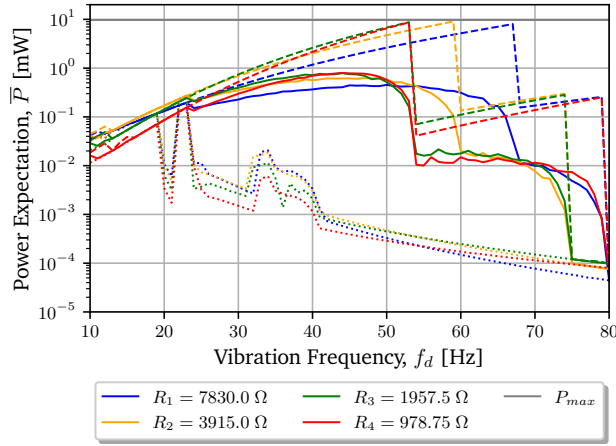

Fig. A.16: Influence of the value of the resistive load on the power expectation for the random strategy (solid lines), for the minimum strategy (dotted lines), and for the maximum strategy (dashed lines) with a constant level of acceleration $A = 2.5$ m.s^{-2}. The horizontal line (in gray) illustrates the power limit of the NVEH given in (13).

dom) strategy is used (dashed (resp. solid) lines), the NVEH power expectation is larger with $R_2 = 3\,915\,\Omega$ (orange dashed (resp. solid) curve) than with $R_1 = 7\,830\,\Omega$ (blue dashed (resp. solid) curve) between 10 and 58 Hz (resp. 53 Hz) because the H1H increases faster with $R_2 = 3\,915\,\Omega$. However, when the vibration frequency reaches 58 Hz, the H1H stops existing if the resistive load is $R_2 = 3\,915\,\Omega$, which explains the observed drop in the power expectation associated with $R_2 = 3\,915\,\Omega$ for random and maximum strategies (solid and dashed orange curves). Similarly, the H1H power with $R_3 = 1\,957.5\,\Omega$ (green dashed curve) is greater than with $R_2 = 3\,915\,\Omega$, but the H1H cutoff frequency becomes substantially smaller (decreasing from 58 Hz to 53 Hz). Therefore, Fig. A.16 shows there is a trade-off between maximizing the H1H power and maximizing the cutoff frequency of H1H

in order to enlarge the harvesting bandwidth. Indeed, a resistance R close to $1/2C_p\omega_d$ maximizes the harvested power[4], but also maximizes the damping induced by the electrical interface. Because of this increased damping, the H1H cutoff frequency tends to be lower, as detailed in [45]. Note that the harvested power curves and cutoff frequencies of other high orbits, such as SH3H, can be explained with similar reasoning. Such analysis shows also that the value of the resistive load might impact both the power associated with each orbit as well as the probability of occurrence of each orbit. For a given vibration frequency, the optimal resistive load is not only the one that maximizes the power of the highest existing orbit, but the one that maximizes the product of the highest existing orbit power with its probability of occurrence. As a matter of example, for $f_d = 50$ Hz, with the random and maximum strategies, the highest orbit is the H1H and therefore the optimal resistance is the one maximizing the product of the H1H power with the H1H probability of occurrence (Fig. 10(a,b)). With the minimum strategy, the optimal resistance is the one maximizing the H1L power (Fig. 10(c)). Therefore, the design of maximum power point trackers (MPPT) algorithms for NVEH seems to be challenging, as it needs to take into account the harvested power with each resistance (similarly as MPPT algorithms for linear harvesters [46, 47]) as well as the probability of the existing orbits with each resistance. Table A.8 summarizes the FoM$_{\overline{P}}$ with the three aforementioned orbit jump strategies for the four resistances.

As shown in Table A.8, a good resistance choice can drastically improve the FoM$_{\overline{P}}$ of the harvester (for example, with the maximum strategy, the FoM$_{\overline{P}}$ grows from 11.90 to 16.49 when adjusting the resistance from $R_4 = 978.75\,\Omega$ to $R_1 = 7\,830\,\Omega$). Table A.8 also demonstrates that $R_2 = 3\,915\,\Omega$ is the optimal resistance for both the random and minimum strategies while $R_1 = 7\,830\,\Omega$ is the optimal resistance for the maximum strategy. Therefore, Table A.8 proves that the optimal resistance for a given NVEH depends on the orbit jump

---

[4]in case of weak coupled NVEH.

	G	G^L	G^H
R_1	2.08	0.17	16.49
R_2	2.44	0.20	16.30
R_3	2.41	0.15	13.23
R_4	2.20	0.09	11.90

Table A.8: FoM$_{\overline{P}}$ values with each orbit jump strategy – random, minimum, maximum – for the four resistive loads $R_1 = 7\,830\ \Omega$, $R_2 = 3\,915\ \Omega$, $R_3 = 1\,957.5\ \Omega$, and $R_4 = 978.75\ \Omega$.

strategy. This is a critical point to consider: to find the best resistive load, one has to take into account the orbit jump strategy that is implemented.

In the following section, we study the effect of the resistive load on the FoM$_{\overline{P}}$. For this study, a range of 28 resistances between 500 Ω and 75 kΩ are considered. The evolution of the FoM$_{\overline{P}}$ is shown in Fig. A.17. When using the NVEH
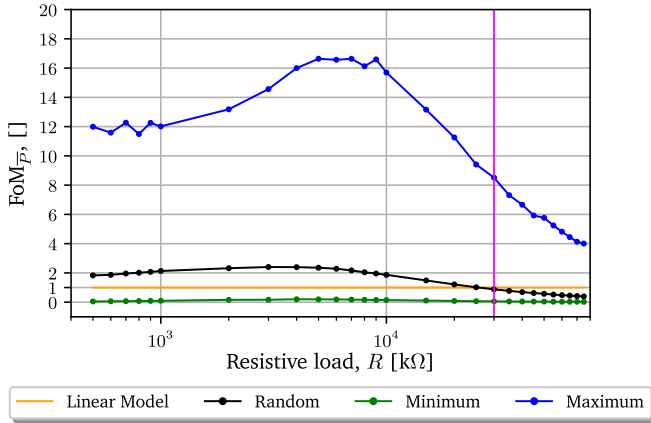

Fig. A.17: FoM$_{\overline{P}}$ for the three orbit jump strategies and FoM$_{\overline{P}}$'s linear equivalent as a function of the resistive load R between 500 Ω and 75 kΩ with a constant acceleration $A = 2.5$ m.s^{-2}. The vertical magenta line corresponds to the resistance where the random strategy becomes lower than the linear model.

with the minimum strategy, its performance is lower to that of its linear equivalent regardless of the value of the resistive load. Moreover, the value of the FoM$_{\overline{P}}$ when using the random strategy is higher than 1 until a threshold resistance at $R = 30$ kΩ (vertical magenta line in the Fig. A.17) where NVEH performance becomes weaker than its linear equivalent. As shown in Fig. A.17, the resistance that maximizes the

FoM$_{\overline{P}}$ and offers the best trade off between power and bandwidth is around 5 kΩ. Optimizing the resistance brings little to no gain if the orbit jump strategy is inefficient (as shown in Fig. A.17 with the minimum strategy). On the other hand, optimizing the resistance makes it possible to greatly enhance the power expectation and the FoM$_{\overline{P}}$ if the orbit jump strategy is efficient (as shown in Fig. A.17 with the maximum strategy).

Figure A.18 shows the maximum power expectation for the three orbit jump strategies. For each vibration frequency, the resistance that maximizes the value of the power expectation is selected. Figure A.18 demonstrates that the bandwidth can be drastically increased with an appropriate tuning of the resistive load value. Table A.9 gives the obtained FoM$_{\overline{P}}$ by tuning the resistance for the three orbit jump strategies. The FoM$_{\overline{P}}$ obtained in Table A.9 are larger than the ones obtained without any resistance adjustment (Table A.8). Note that the improvement of the maximum strategy FoM$_{\overline{P}}$ is particularly significant, which proves the interest in implementing adaptative electrical interfaces with MPPT algorithms along with efficient orbit jump strategies.
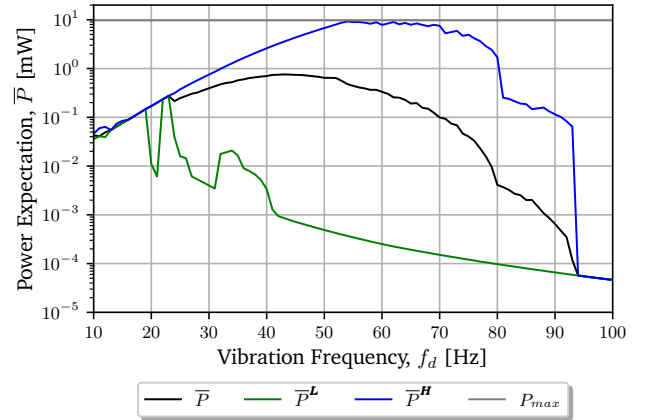

Fig. A.18: Maximum power expectation curves (obtained by selecting the optimal resistance for each vibration frequency) for each ICs grid with $A = 2.5$ m.s^{-2}. The horizontal line (in gray) illustrates the power limit of the NVEH given in (13).

19

	G	G^L	G^H
R_{opt}	3.37	0.24	36.93

Table A.9: Maximum $\text{FoM}_{\overline{P}}$ with each orbit jump strategy – random, minimum, maximum – using the optimal resistance.

Appendix A.2. Evolution of the $\text{FoM}_{\overline{P}}$ with the electromechanical coupling

We study the influence of the electromechanical coupling on the power expectation and $\text{FoM}_{\overline{P}}$. The expression of the electromechanical coupling is given in (A.1) (as detailed in [32]).

$$k_m^2 = 4\left(\frac{x_0}{L}\right)^2 \frac{\alpha^2}{M C_p \omega_0^2} \qquad (A.1)$$

Figure A.19 shows the power expectation curves for $k_m^{2\,(1)} = 0.7\%$, $k_m^{2\,(2)} = 2.8\%$, $k_m^{2\,(3)} = 6.3\%$ and $k_m^{2\,(4)} = 11.1\%$. When the maximum (resp. random) strategy is used (dashed (resp. solid) lines), the power expectation of the NVEH is greater between 10 and 47 Hz (resp. 41 Hz) with the strongest electromechanical coupling, $k_m^{2\,(4)} = 11.1\%$ (red curves) because electrical damping is more important with $k_m^{2\,(4)} = 11.1\%$. However, this strong electromechanical coupling leads to significant electrical damping which explains why the H1H stops existing at a relatively low frequency (47 Hz). The power expectations associated with the maximum strategy (dashed lines) illustrate that the cutoff frequency of H1H increases with a lower electromechanical coupling. Such analysis shows that the value of the electromechanical coupling can influence both the power associated and the probability of occurrence of each orbit. Table A.10 summarizes the $\text{FoM}_{\overline{P}}$ with the three strategies for the four tested electromechanical couplings. As shown in Table A.10, the electromechanical coupling has a great impact on the value of the $\text{FoM}_{\overline{P}}$. As a matter of example, with the random strategy, the $\text{FoM}_{\overline{P}}$ can increase from 0.80 to 2.83 with a larger value of the electromechanical coupling from $k_m^{2\,(1)} = 0.7\%$ to $k_m^{2\,(4)} = 11.1\%$. With the maximum strategy, the $\text{FoM}_{\overline{P}}$ grows from 8.05 to 17.15 with a larger electromechanical coupling from $k_m^{2\,(1)} = 0.7\%$ to $k_m^{2\,(3)} = 6.3\%$. That means that the op-
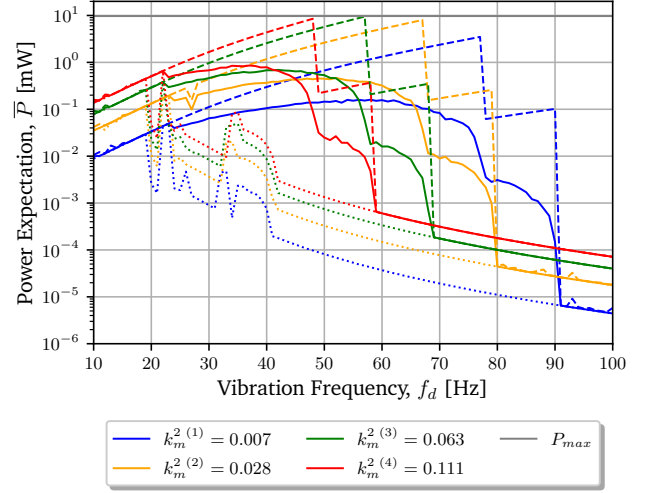

Fig. A.19: Influence of the electromechanical coupling on the power expectation for the random strategy (solid lines), for the minimum strategy (dotted lines), and for the maximum strategy (dashed lines) with $A = 2.5$ m.s^{-2}. The horizontal line (in gray) illustrates the power limit of the NVEH given in (13).

	G	G^L	G^H
$k_m^{2\,(1)}$	0.80	0.04	8.05
$k_m^{2\,(2)}$	2.08	0.16	16.46
$k_m^{2\,(3)}$	2.71	0.31	17.15
$k_m^{2\,(4)}$	2.83	0.52	13.24

Table A.10: $\text{FoM}_{\overline{P}}$ value with each orbit jump strategy – random, minimum, maximum – for the four electromechanical couplings $k_m^{2\,(1)} = 0.7\%$, $k_m^{2\,(2)} = 2.8\%$, $k_m^{2\,(3)} = 6.3\%$ and $k_m^{2\,(4)} = 11.1\%$.

timal electromechanical coupling depends on the orbit jump strategy that is implemented.

The evolution of the $\text{FoM}_{\overline{P}}$ as a function of the electromechanical coupling is shown in Fig. A.20. When the minimum strategy is considered the $\text{FoM}_{\overline{P}}$ is always smaller than 1, regardless of the electromechanical coupling. Figure A.20 shows that with the random strategy, for a weak electromechanical coupling between 0.5 % and 1 %, the NVEH $\text{FoM}_{\overline{P}}$ is lower than 1 and is therefore lower than its linear equivalent. From $k_m^2 = 1\%$ (indicated by the magenta line in Fig. A.20), the random strategy $\text{FoM}_{\overline{P}}$ becomes larger than the linear model $\text{FoM}_{\overline{P}}$. Figure A.20 shows that the maximum strategy $\text{FoM}_{\overline{P}}$ always remains greater than the linear $\text{FoM}_{\overline{P}}$,
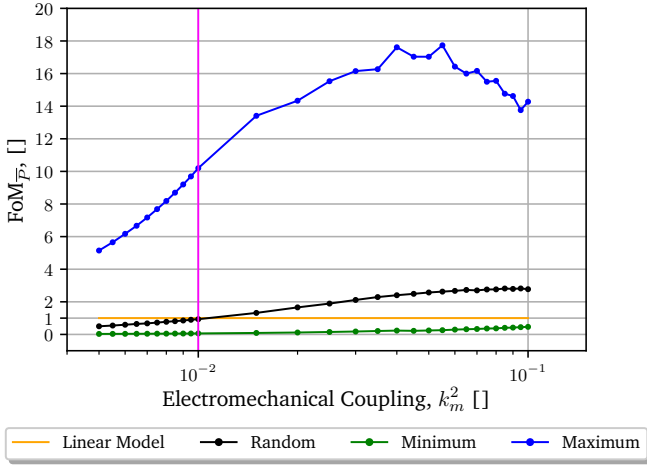
Fig. A.20: Evolution of the FoM$_{\overline{P}}$ for the three strategies and FoM$_{\overline{P}}$'s linear equivalent as a function of the electromechanical coupling k_m^2 between 0.5 % and 10 %. The vertical magenta line corresponds to the electromechanical coupling where NVEH performance with random strategy increases in comparison to the linear model.

and is maximized when the electromechanical is around 5 %. Note that if the resistive load is tuned and optimized (as in Fig. A.18), the FoM$_{\overline{P}}$ would always be larger with a stronger electromechanical coupling.